Seasonal and inter-annual changes in the surface chlorophyll of the South China Sea

Palacz, Artur P.; Xue, Huijie; Armbrecht, Carrie; Zhang, Caiyun; Chai, Fei

Published in:
Journal of Geophysical Research: Atmospheres

Link to article, DOI:
10.1029/2011JC007064

Publication date:
2011

Document Version
Publisher's PDF, also known as Version of record

Seasonal and inter-annual changes in the surface chlorophyll of the South China Sea

Artur P. Palacz,[1] Huijie Xue,[1] Carrie Armbrecht,[1] Caiyun Zhang,[2] and Fei Chai[1]

Received 17 February 2011; revised 9 June 2011; accepted 21 June 2011; published 16 September 2011.

[1] The Hilbert-Huang Transform was applied to the satellite-derived monthly surface chlorophyll-*a* data and monthly blended satellite wind products from September 1997 to April 2010 to examine temporal trends in these time series. Using this new approach, we found an overall increasing trend in both the surface chlorophyll-*a* concentration and surface wind speed averaged over the entire South China Sea. Chlorophyll-*a* concentration increased by 12% between September 1997 and September 2003, and then decreased by 3% by April 2010. Wind speed increased by 21% between September 1997 and December 2005, but then decreased by 11%. The increasing trends followed by a period of decrease in both chlorophyll-*a* and wind speed time series are likely driven by the El Niño Southern Oscillation signal. The biggest change occurred in the deep basin region where the area averaged chlorophyll-*a* concentration increased by 20% between 1997 and 2010. This trend was primarily attributed to a 19% increase of the surface area of waters with monthly averaged chlorophyll-*a* concentration greater than 0.2 mg m^{-3}, called the high chlorophyll waters. The most pronounced change occurred in winter with the high chlorophyll surface area expanding from 56 to 64% of the South China Sea. Strong correlation between chlorophyll-*a* and wind speed in this region suggested that it is the enhanced wind-induced mixing in the winter that stimulates phytoplankton growth via increased vertical supply of nutrients. The obtained 13-year trends indicate that the physical-biological interactions also take place on inter-annual time scales in the South China Sea.

Citation: Palacz, A. P., H. Xue, C. Armbrecht, C. Zhang, and F. Chai (2011), Seasonal and inter-annual changes in the surface chlorophyll of the South China Sea, *J. Geophys. Res.*, *116*, C09015, doi:10.1029/2011JC007064.

1. Introduction

[2] Despite the known limitations of using the surface chlorophyll-*a* concentration (Chl-*a*) as a proxy for biological productivity [e.g., *Balch and Byrne*, 1994], it remains the one of the best available approaches to evaluate physical and biological interactions in the ocean. More than a decade has passed since the Sea-viewing Wide Field-of-view Sensor (SeaWiFS) mission started providing the oceanographic community with high spatial and temporal resolution of surface Chl-*a* estimates. This information is particularly valuable in studying variability of primary productivity in responses to physical processes, especially in dynamic regions such as marginal seas. Exhibiting large seasonal and inter-annual variability, these regions are difficult to study with the available in situ observations alone.

[3] The South China Sea (SCS) is one of the largest marginal seas in the western Pacific Ocean, extending from the equator to 23°N and from 99° to 120°E. The hydrodynamic distinctiveness of the basin is determined by its large size, semi-enclosed nature and complex geometry [*Xue et al.*, 2004]. The SCS is sensitive to many types of physical forcing on the short-term (e.g., internal waves and tides, mesoscale eddies, typhoons, etc.) [*Liu et al.*, 1998; *Wang et al.*, 2009; *Xiu et al.*, 2010], annual (monsoon) [*Wyrtki*, 1961; *Shaw and Chao*, 1994; *Chu et al.*, 1997], inter-annual (e.g., El Niño) [*Chao et al.*, 1996; *Chen et al.*, 2010], and long-term (e.g., climate change) scales [*Ning et al.*, 2009]. The seasonally reversing East Asian Monsoon that alternates between the winter northeasterly wind and the summer southwesterly wind, exerts a primary control on the physical-biological interactions of the SCS [e.g., *Wu et al.*, 1998; *Ning et al.*, 2004; *Wong et al.*, 2007]. Inter-annual variability in hydrographic and biogeochemical conditions is primarily associated with the El Niño Southern Oscillation (ENSO) cycle [*Zhao and Tang*, 2007; *Kuo et al.*, 2008; *Ning et al.*, 2009]. Strong ENSO events result in an anomalous Hadley circulation that causes not only variations in the sea surface wind, air temperature, and freshwater cycle [*Zong et al.*, 2010], but also in sea surface temperature [*Wang et al.*, 2003].

[4] Observational and modeling studies have consequently shown that the monsoons largely control patterns of chlorophyll-*a* distribution in the SCS [*Liu et al.*, 2002; *Tang et al.*, 2004; *Liu and Chai*, 2009; *Chai et al.*, 2009]. The seasonal cycle of domain-averaged Chl-*a* in this marginal sea varies from roughly 0.02 to 0.2 mg m^{-3} [*Liu and Chai*, 2009; *Chai et al.*, 2009]. Although winter is the most productive season of the year with a peak of 0.2 mg m^{-3} in January, there

[1]School of Marine Sciences, University of Maine, Orono, Maine, USA.
[2]State Key Laboratory of Marine Environmental Science, Xiamen University, Fujian, China.

0148-0227/11/2011JC007064

is a secondary peak in the summer with values reaching 0.1 mg m^{-3} in August [*Liu et al.*, 2002]. In winter, increased wind stimulates photosynthesis through strong mixing that entrains the nutrient rich deep water to the upper sunlit layer. There is additional evidence of winter upwelling in the northeastern part of the SCS and northwest of Luzon [*Chao et al.*, 1996; *Liu et al.*, 2002; *Chen et al.*, 2006]. In summer, the upper water column is stratified, which results in nutrient limitation and reduction in biological productivity. However, the summer chlorophyll increase is mostly fostered by the upwelling-favorable winds, especially near the coastal regions.

[5] In this paper we analyzed the satellite-derived surface Chl-*a* and wind speed monthly records and looked at interannual concurrent trends in physical forcing and primary productivity in the SCS. By applying the Hilbert-Huang Transform (HHT) [*Huang et al.*, 1998; *Huang and Wu*, 2008] we separated the time series into high and low frequency variability signals by means of empirical mode decomposition that enables a more powerful approach to trend analysis. Through identifying a trend that is a nonlinear property of the time series, we intended to better understand how the SCS responds to the observed climate changes in the western Pacific.

2. Methods

[6] In this study, the SCS was treated as a rectangular box between 1°N and 25°N latitude and 104°E and 120°E longitude. Surface Chl-*a* was obtained from the 9-km pixel resolution, monthly averaged SeaWiFS Level-3 data (ftp://oceans.gsfc.nasa.gov/SeaWiFS/). Sea surface wind products were derived from monthly averaged vectors blended from multiple satellite observations [http://www.ncdc.noaa.gov/oa/rsad/air-sea/seawinds.html] including Scatterometer (QuikSCAT), Special Sensor Microwave/Imager (SSM/I), Tropical Rainfall Measuring Mission (TRMM) Microwave Imager (TMI) and the Advanced Microwave Scanning Radiometer (AMSR-E) in a global domain with 0.25° resolution, decomposed into zonal and meridional components using the National Centers for Environmental Prediction (NCEP) Re-analysis 2 (NRA-2) scheme [*Zhang et al.*, 2006]. Monthly time series spanned from September 1997 to April 2010. Gaps in the Chl-*a* time series (February and March 2008, May 2009) were due to problems with geo-positioning of the imagery data reported by the satellite mission, and were substituted with the climatological monthly means calculated based on the same records.

[7] We began by examining the temporal trends in the SCS domain-averaged surface Chl-*a* concentration (in mg m^{-3}). The next step relied on two criteria to divide the SCS into subregions. To distinguish between shelf waters (less than 500-m depth) and deep basin waters (greater than 500-m depth) we used the bathymetry from the ETOPO5 global relief (http://www.ngdc.noaa.gov/mgg/global/etopo5.html) supplied by the National Oceanic and Atmospheric Administration (NOAA) National Geophysical Data Center (NGDC). We then compared the changes in area-averaged surface Chl-*a* concentration between the shelf and deep basin waters. Furthermore, we used the limit of 0.2 mg-Chl-*a* m^{-3} to separate waters of low and high surface chlorophyll concentration. We then calculated the surface area of the low and high Chl-*a* waters and estimated their rates of changes.

[8] Time series analyses were performed using linear regression and the HHT - a newly developed adaptive data analysis method that has already been successfully used in geophysical research [*Huang and Wu*, 2008, and references therein]. HHT consists of empirical mode decomposition (EMD) and Hilbert spectral analysis. In this study we did not apply the Hilbert spectral analysis but instead focused on data analysis using EMD, which decomposes complex data series into a finite number of intrinsic mode functions (IMFs), and a residual trend that is an intrinsically determined monotonic function, or a function with at most one extreme [*Wu et al.*, 2007]. Each IMF must satisfy two conditions. First, in the whole data set, the number of extrema and the number of zero crossings in each must either equal or differ at most by one. Second, at any data point, the mean value of the envelope constructed around the local maxima and the envelope constructed around local minima of each constituent is zero. The process of defining envelopes around local maxima and minima, and extracting IMFs is called sifting. In order to extract each IMF, sifting is carried out iteratively until reaching a stoppage criterion, defined by the approximate local envelope symmetry condition in the sifting process [*Huang and Wu*, 2008]. *Huang et al.* [1999, 2003] proposed a second type of criterion, termed the S stoppage. With this type of stoppage criterion, the sifting process stops only after the numbers of zero crossings and extrema are (1) equal or at most differ by one; and (2) stay the same for S consecutive times.

[9] The adaptive and hence very efficient technique of EMD is applicable to nonlinear and non-stationary processes, providing IMFs with physically meaningful interpretations of both linear and nonlinear phenomena [*Huang et al.*, 1998]. This aspect of EMD constitutes its advancement over most of the traditional time series analysis techniques, including the Empirical Orthogonal Function (EOF) analysis [*Huang et al.*, 1998]. Here we applied the improved white noise-assisted decomposition method of ensemble empirical mode decomposition (EEMD), which is equivalent to an artificial ensemble mean of EMDs, described in detail by *Wu and Huang* [2009]. EEMD requires two input parameters: the amplitude of added white noise (An), and the number of ensembles (Nesb). The amount of white noise added is expressed as the ratio of standard deviation of noise to standard deviation of the original signal. Higher (lower) noise amplitude in EEMD provides better identification of lower (higher) frequency IMFs. The number of ensembles needs to be large enough to eventually cancel out the added noise and small enough to make this data analysis method computationally efficient. Optimization of An and Nesb for different geophysical data was studied by *Wu and Huang* [2009]. We performed a similar optimization in this study.

[10] Additional post-processing techniques were employed in order to guarantee that the extracted IMFs are 'true IMFs,' i.e., their number of extrema does not differ from the number of zero crossings by more than 1 for any given IMF [*Huang et al.*, 2003]. *Wu and Huang* [2009] describe the post-processing as follows: Direct output of the initial decomposition is reprocessed with the combination of its components and an additional EMD calculation. When applied to com-

ponents that are adjacent in the frequency domain, it is possible to eliminate mode mixing and render a whole set of true IMFs. In particular, you will need to extract one IMF and add the remainder to the next component. Then, you calculate EMD again on the sum of the remainder and the next component from the original decomposition. This procedure is carried out consecutively until obtaining just the residual trend.

[11] In this investigation, evaluation of the results from EEMD with post-processing was conducted by: (1) adding confidence limits to all identified IMFs; (2) testing the "goodness" of the IMFs by calculating the number of excessive extrema; and (3) estimating the statistical significance of the IMFs. Confidence limits reflect the distance of one standard deviation around the mean obtained from a number of decompositions with a variable S stoppage criterion. Here we varied the S value to generate a few different sets of IMFs by imposing a weaker or more stringent constraint on how smooth the mean envelope around local extrema is. The mean and the spread of corresponding IMFs was then calculated to determine the confidence limit quantitatively, as described by *Huang et al.* [2003], and in a review by *Huang and Wu* [2008].

[12] There are two standard ways of evaluating the "goodness" of IMFs: (1) orthogonality index; and (2) number of excessive extrema, the latter of which was applied in this study. In principal, the number of extrema of a true IMF should not differ from its number of zero crossings by more than 1. While not all IMFs were rendered good after the initial EEMD calculations, all the IMFs were deemed to be good after applying the post-processing procedures described above.

[13] Statistical significance of IMFs is based on the distribution of energy as a function of mean period of the IMF relative to that of pure white noise. This method allows one to differentiate true signals from components of noise with any selected statistical significance level (90%, 95%, or 99%) [*Wu and Huang*, 2004, 2005; *Huang and Wu*, 2008]. We combined the statistically significant, lowest frequency modes with the residual trend in order to quantitatively compare patterns of inter-annual variability with the ENSO signal. *Tsui et al.* [2010] adopted a similar approach by empirically treating the lowest-frequency components (including the residual) as the signal trend. This approach is motivated by the preference to explain intrinsic trends on one or two inclusive time scales [*Wu et al.*, 2007]. This procedure does not undermine the statistical significance of EEMD. In fact, the statistical significance of such a combined signal usually increases. Such a combined, true IMF was then assigned a physical meaning based on its quasiperiodicity.

[14] We were able to assign a physical meaning to every IMF that was statistically significant at a 90% confidence level or higher. Insignificant IMFs, usually 3rd and 4th IMFs, were interpreted as noise inherent to the original signal. The final set of IMFs decomposed through EEMD was obtained by optimizing An and Nesb parameters to minimize the number of excessive extrema while maintaining high statistical significance of IMFs. In order to better resolve the signals with highest amplitude of variability (intraseasonal and annual) in Chl-*a* and (intraseasonal and quasi-annual) wind products, An was set at relatively low level, between 0.1 and 0.2, while Nesb was kept consistently high between 500 and 700.

3. Results and Discussion

3.1. Domain-Averaged Surface Chlorophyll and Wind Speed Distribution

[15] The results of EEMD performed on the SCS domain-averaged Chl-*a* and surface wind speed time series are presented in Figure 1. The full decomposition was included to illustrate the high to low frequency progression with which EEMD extracts periodic signal components (IMFs: C1–C6). Statistically significant IMF components were assigned a physical meaning based on the interpretation of their mean period. In Figure 2 IMFs were distributed with respect to their period and statistical significance. We classified C1 (statistically significant at 99% level, Figure 2) as representing intraseasonal variability (Figure 1). C1 in the wind speed time series was unlikely to reflect storm activities because our analysis could not resolve variability with periods less than two months. Corresponding C1s from Chl-*a* and wind speed were relatively well correlated and statistically significant with $r = 0.49$ and $p < 0.01$ (Table 1). C2 was statistically significant at 99% level for both Chl-*a* and surface wind speed (Figure 2). While C2 from the Chl-*a* time series was attributed to a regular annual cycle, indicated by the characteristic winter absolute maxima around December each year (Figure 1), C2 from the wind speed time series showed more scale mixing and was thus interpreted as a quasi-annual variability. Both C2s were well correlated with a correlation coefficient of 0.62 and a p-value less than 0.01 (Table 1). As expected, C2 accounted for most of the total variability in both time series. Moreover, the adaptive and intrinsic nature of EEMD enabled detection of the inter-annual differences in the magnitude of the annual cycle. Specifically, the annual cycle of Chl-*a* was most pronounced between 1999 and 2000 and least pronounced in the 2002–2004 period. Similar observations in the wind speed signal decomposition revealed particularly strong annual cycles between 1998 and 2001, and later in 2007 and 2010. As expected, the major annual Chl-*a* anomalies, expressed in C2, were most likely driven by changes in the monsoon circulation, which is indicated by stronger or weaker wind speeds. Moreover, small discrepancies (+/−2 months) in the onset of winter Chl-*a* peaks were detected, possibly related to the shift in the time of arrival of the northeast monsoon (Figure 1). Such observations were not possible using most traditional time series analysis methods that assume a steady seasonal or annual cycle.

[16] In order to evaluate whether the results shown in Figure 1 exhibit any artifact of possible boundary (end) effects in our analysis, we truncated the time series to start in January 1999 and end in January 2009, and repeated the EEMD analysis. The amplitude of the C2 oscillations in winter 1999 and 2009 (new end peaks) matched with the peaks of corresponding years from the original, longer time series, indicating a lack of visible boundary effects in this frequency range. A relatively weak winter Chl-*a* peak in 1998 (the beginning of the time series) was then attributed to weaker wind circulation associated with the positive ENSO phase reported for that year [*Kuo et al.*, 2008].

[17] Lower frequency oscillation in C4 was not statistically significant. While both C5 and C6 were statistically signifi-

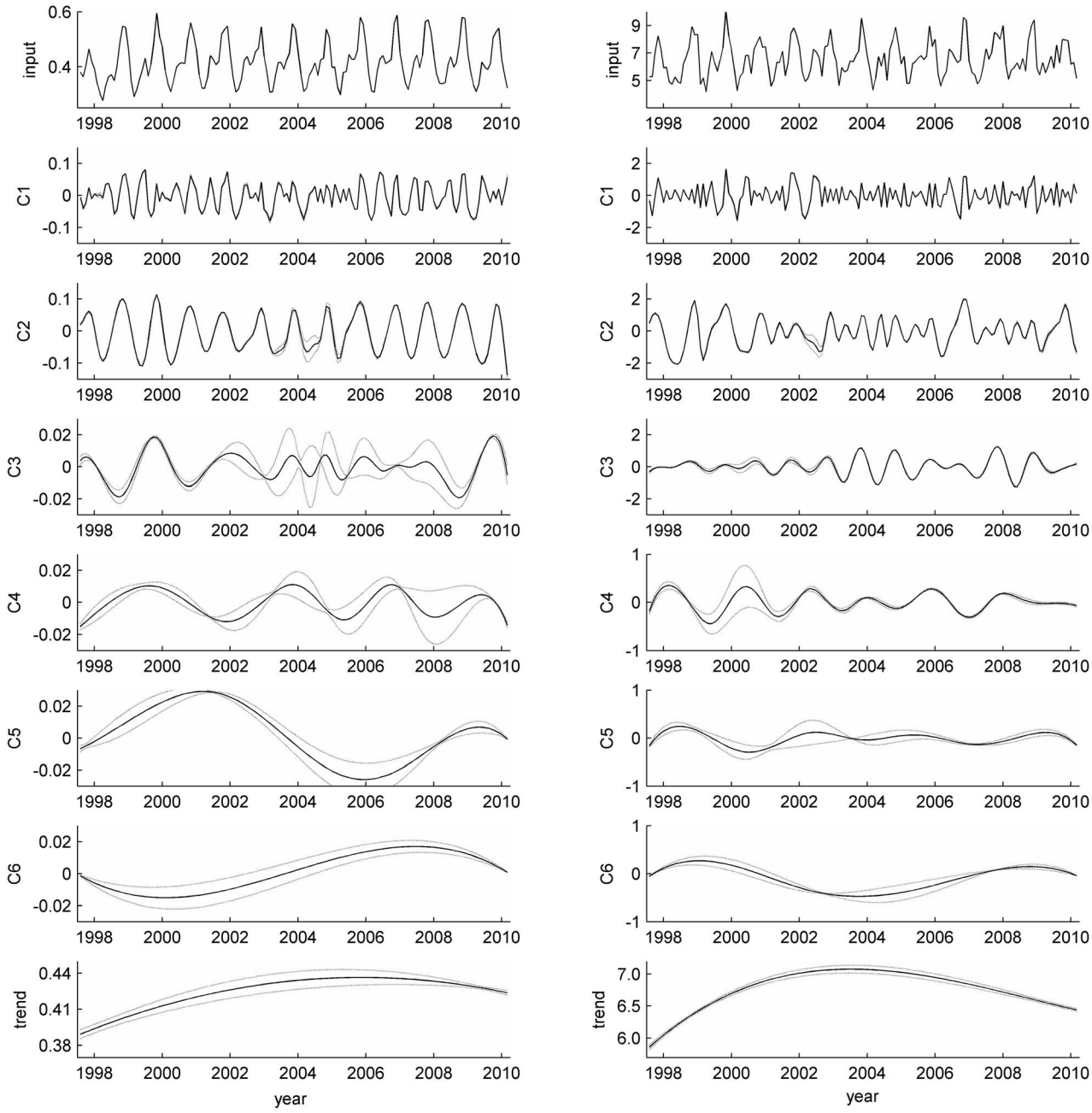

Figure 1. EEMD applied to the domain-averaged (left) SeaWiFS Chl-*a* [mg m^{-3}] and (right) blended surface wind speed [m s^{-1}]. The input shown in the top panels corresponds to the Chl-*a* and wind speed raw data. The extracted intrinsic mode functions (C1–C6) and the residual trend are displayed on the remaining panels from top to bottom. Confidence limits are marked with thin dashed lines and represent a range of one standard deviation calculated from several EEMD analyses, with a varied S criterion.

cant in the Chl-*a* time series, only C6 was significant in the wind speed time series. A careful look at Figure 2 revealed a close match in the average period of C5 in Chl-*a* and C6 in wind speed time series. These two IMFs were also significantly correlated ($r = 0.25$, $p < 0.01$). On the other hand, there was no significant correlation between C6 obtained from the two time series, with $p > 0.5$ (Table 1). After combining C5, C6 and the residual trend the Chl-*a*, and C6 and the residual trend from the wind speed, we observed that within the September 1997 to April 2010 time period there were two local maxima and three local minima in this frequency range (Figure 3). This pattern was in good agreement with patterns of inter-annual variability recorded in the raw Multivariate ENSO index (MEI) time series [http://www.esrl.noaa.gov/psd/], here presented on its reversed scale for better comparison (Figure 3). There was a high positive and statistically significant correlation between the reversed MEI and surface wind speed ($r = 0.76$, $p < 0.01$) and a lower but also statistically significant correlation between the reversed MEI and Chl-*a* ($r = 0.31$, $p < 0.01$) throughout the 13-year time period

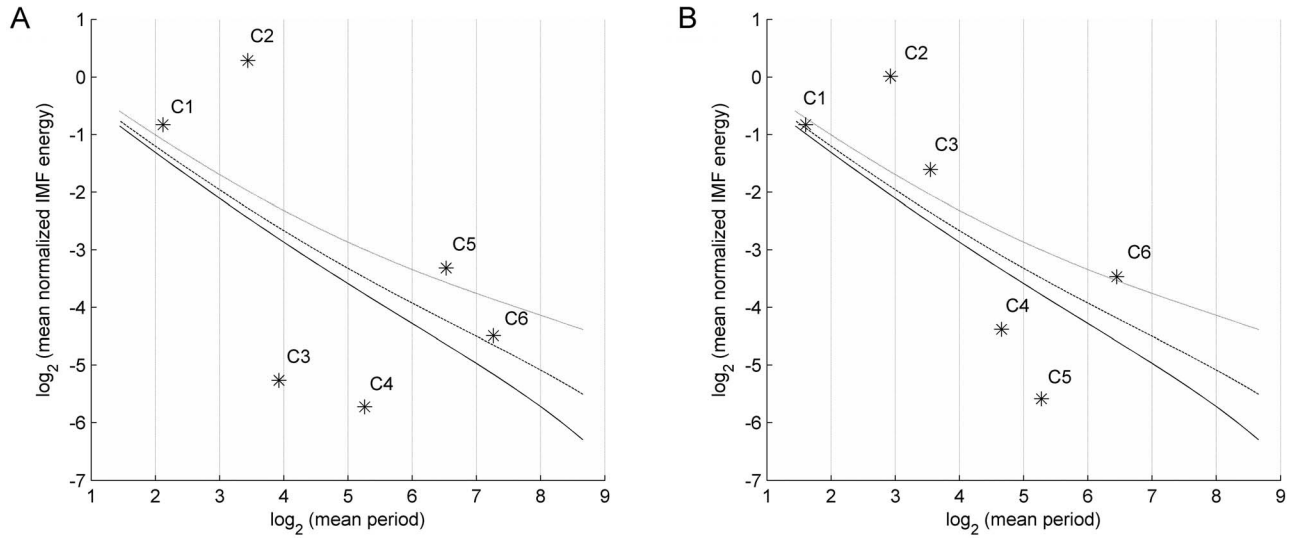

Figure 2. Statistical significance tests performed on the EEMD of the domain-averaged (a) Chl-*a* and (b) surface wind speed. The diagram plots the energy of an IMF as a function of its period [months] on a $\log_2$ scale. Statistically significant IMFs are placed above the diagonal lines, for 99% (grey solid line), 95% (dashed line) or 90% significance level (black solid line). IMFs are labeled consistently with the constituent number assigned in Figure 1.

(Table 1). Strong positive MEI anomalies (negative reversed MEI anomalies) were recorded through autumn 1997 and winter 1998, between winter 2002 and 2005, and again throughout 2009. In summary, we concluded that the statistically significant, low-frequency signals in both Chl-*a* and wind speed were likely a result of the strong ENSO-driven teleconnection between the equatorial Pacific and the SCS physical circulation and biogeochemical cycling [*Chao et al.*, 1996; *Klein et al.*, 1999; *Xie et al.*, 2003; *Gu et al.*, 2010; *Chen et al.*, 2010].

[18] Even though there is no published evidence for the link between the 2009–10 El Niño and changes in the hydrography of the SCS, our results revealed the conditions analogous to the effects of the 1997–98 El Niño [*Zhao and Tang*, 2007; *Xie et al.*, 2009; *Jing et al.*, 2011]. *Zhao and Tang* [2007] reported that Chl-*a* concentrations in 1998 summer in the SCS were the lowest among the seven years. They concluded that this anomalous event of low phytoplankton biomass was the result of dramatic changes in atmospheric and oceanic circulation in the SCS (weaker southwesterly monsoon winds and offshore currents), coinciding with an El Niño year in 1998. On the other hand, *Jing et al.* [2011] found contrasting results in the northern SCS, where stronger upwelling and higher Chl-*a* concentrations were observed in the summer of 1998. They concluded that while the northern flank of atmospheric circulation anomaly intensified the monsoonal winds off the northern SCS coast, the southern flank suppressed the southwesterly winds off the coast of Vietnam.

[19] The residual signal (obtained after extracting all IMFs from the original time series) revealed a 13-year trend, specific to the September 1997–April 2010 period. For domain-averaged surface Chl-*a* concentration the trend showed a small 0.04 mg m^{-3} (9%) increase over the time period (Figure 1). The domain-averaged surface wind speed increased by approximately 0.6 m s^{-1}, or 10% between September 1997 and April 2010 (Figure 1). Although these inter-annual changes are low in magnitude, they revealed interesting basin-wide patterns.

[20] These trends, defined as adaptive, local and intrinsic [*Wu et al.*, 2007], were non-monotonic and displayed a 12% maximum Chl-*a* and 21% maximum wind speed increase till mid 2003 and end of 2005, respectively. These increases were then followed by several percent decreases through beginning of 2010. In order to compare the results of EEMD analysis with linear regression, we removed the annual cycle (C2) from the input time series. We found a statistically significant 6% increase in the Chl-*a* concentration and surface wind speed between September 1997 and April 2010. These rates

Table 1. Results of Regression Analysis Performed on Different Scales of Temporal Averaging of the SeaWiFs Chl-*a* [mg m^{-3}], Blended Sea Winds Surface Wind Speed [m s^{-1}] Averaged Over the Entire SCS Domain, and the Multivariate ENSO Index (MEI)[a]

Time Series Compared	R	P-Value
Chl-a Versus Wind Speed		
Annual average	0.78	<0.01
Monthly average	0.90	<0.01
Winter average	0.76	<0.01
Summer average	0.77	<0.01
C1 (intraseasonal)	0.49	<0.01
C2 (annual or quasi-annual cycle)	0.62	<0.01
C6 (inter-annual)	−0.15	>0.05
trend	0.80	<0.01
Chl-a Versus MEI		
C5+C6+trend	0.31	<0.01
Wind Speed Versus MEI		
C6+trend	0.76	<0.01

[a]C2 represents the quasi-annual cycle extracted using EEMD, and 'trend' is the residual obtained also through EEMD. The combination of C5, C6 and trend (Chl-*a*) or C6 and trend represents the low-frequency variability identified through EEMD and compared to the raw MEI index.

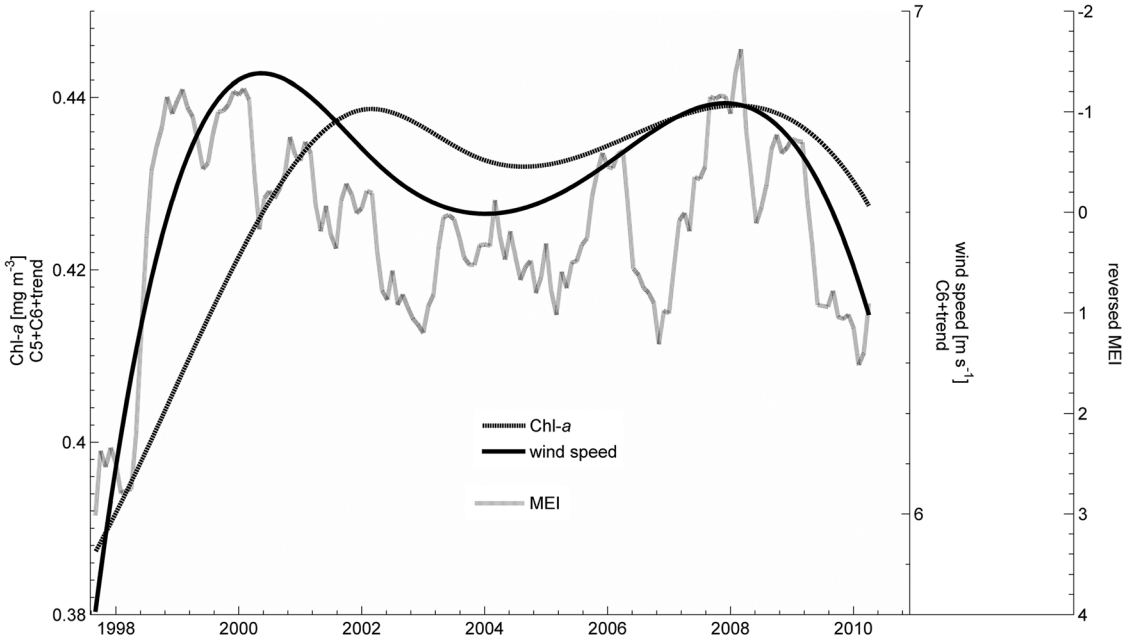

Figure 3. Combined statistically significant, low frequency oscillations and the residual trend from the EEMD analysis performed on the domain-averaged Chl-a [mg m^{-3}] (black solid line) and surface wind speed [m s^{-1}] (dashed line), compared to the reversed raw MEI (grey solid line) between September 1997 and April 2010.

of increase were only slightly lower than the ones revealed through EEMD (9% and 10%, respectively) but failed to account for the nonlinearity of the overall trend. In general, the residual trend via HHT confirmed the presence of a strong link between physical and biological changes in the SCS.

[21] It is unlikely that the trends were artifacts of any end effects of the extracted IMFs. First, EEMD represents an improvement over EMD in ameliorating the end effects due to the fact that added noise helps distribute the end slopes more uniformly across an ensemble, thus avoiding a deterministic drift in any direction [*Wu and Huang*, 2009]. Second, the confidence limits added to the analysis in this study provided a means of estimating the sensitivity to the chosen value of S and the discrepancy of frequency decomposition at the ends of time series using a different S. In most IMFs shown in Figure 1, the spread of variance at the ends of the time series was negligible. Additionally, we carried out sensitivity studies to test how different values of An and Nesb affected the boundary behavior of all IMFs (not shown). While those IMFs that were consistently determined as statistically insignificant (C3 and C4) displayed noticeable changes in their shape and average period in response to very different levels of white noise added (e.g., 0.1 vs 0.7), there were little changes observed in the shape of the residual trend. Furthermore, we conducted EEMD on a truncated time series and confirmed that the shape of the 13-year trend was driven by two strong El Niño events in 1997–98 and 2009–10, and not by end effects. It is thus a coincidence that the largest variability was observed at the beginning and the end of our time series.

[22] The results of EEMD analysis also allowed us to conclude that the observed 13-year trend might in fact be part of a longer, decadal cycle that controls the physical and biogeochemical regime in the SCS. *Ning et al.* [2009] used physical and chemical oceanographic data obtained from combined in situ and satellite observations during 1976–2004 to identify long-term changes in the ecosystem in the northern SCS. In another study by *Xue et al.* [2010], analyses of the 1990–2010, area-averaged, result from a Pacific ROMS model, remote sensing products including sea surface wind, as well as in situ observations from the World Ocean Database (http://www.nodc.noaa.gov/OC5/WOD/pr_wod.html), pointed at the 1997/1998 El Niño event as an inflection point within the observed inter-decadal trend within the SCS basin. In summary, several investigations pointed out a possible regime shift that might have occurred after the 1997–98 El Niño [*Ning et al.*, 2009; *Liu and Chai*, 2009; *Xue et al.*, 2010].

3.2. Patterns in Sub-Regional Distribution of Chl-*a*

[23] In Figure 4 we presented the results of EEMD analysis performed on the surface Chl-*a* averaged over the shelf and deep basin regions of the SCS that are divided by the 500-m isobath. Here we only included the residual trend (with confidence limits) placed on top of the original monthly averaged time series. The annual mean surface chlorophyll concentration equaled 0.6 mg m^{-3} in the shelf (Figure 4a), which was much higher than the annual mean of 0.14 mg m^{-3} found in the deep basin (Figure 4b). The winter Chl-*a* maximum was consistently higher than the summer values in the entire SCS. This pattern was less visible in the deep basin in the anomalous year 1998, whose seasonality was strongly altered by the El Niño event. A marked increase in the deep basin averaged Chl-*a* concentration was detected for the first 11 years of the time series after which we noted a small decrease. The trend in the shelf Chl-*a* revealed a similar yet

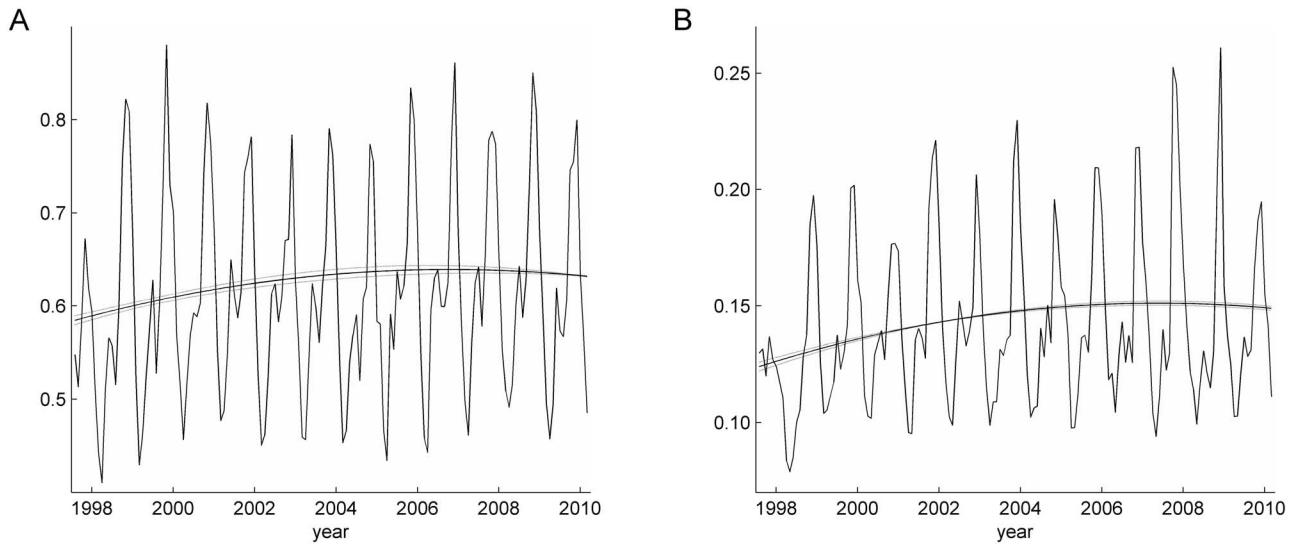

Figure 4. EEMD applied to the SeaWiFS Chl-*a* [mg m^{-3}] averaged over the (a) shelf region and (b) deep basin region of the South China Sea. The original time series are shown together with the residual trends and the confidence limits (grey solid lines).

relatively less pronounced initial increase followed by a decrease after 2006. Between September 1998 and April 2010, Chl-*a* in the shelf region increased by 8% and in the deep basin region by 20%. These findings revealed the large inter-annual change in Chl-*a* within the deep basin of the SCS. We concluded that the high initial rate of increase in Chl-*a* was likely a result of a shift that took place after the 1997–98 El Niño. Another strong positive ENSO phase was recorded in the winter 2009–10 and likely caused an offset in this 13-year trend, resulting in an overall non-monotonic trend with a local maximum around winter 2008 (Figure 4b). The strong effect of ENSO in the deep basin of the SCS was also revealed through the statistically significant C5 and C6 IMFs, with a mean period of ~7 years (the maximum ENSO period [*MacMynowski and Tziperman*, 2008]). We found no corresponding signal of similar frequency in the shelf region, which further emphasized the importance of the deep basin in the SCS dynamics. This explanation was confirmed by a constant increasing trend obtained from EEMD performed on a shorter time series of the deep basin region, ending in December 2008. Furthermore, we concluded that the majority of inter-annual changes in the SCS took place in the deep basin region. 11% increase in the surface wind speed over the deep basin region between September 1997 and January 2005 (not shown) confirmed the close link between the wind circulation and Chl-*a* distribution on these extended inter-annual time scales.

[24] To further examine changes in the spatial distribution of the Chl-*a* in the SCS, we applied the EEMD separately to the low and high chlorophyll sub-regions. These sub-regions were separated by the 0.2 mg m^{-3} contour, which when calculated as the mean over the 1998–2009 period was found to coincide closely with the 500 m isobath (Figure 5a). Out of the 6 IMFs obtained after performing EEMD, we attributed a physical meaning to C1, C2, and C6, which were all statistically significant. The remaining IMFs, that are statistically insignificant, represent noise in the time series and their mean periods cannot be attributed to any signals of known physical processes. In Figure 6 we included the original time series together with the residual trends for area-averaged Chl-*a* concentration (Figures 6a and 6c) and for the % of total surface area occupied by the high and low chlorophyll waters (Figures 6b and 6d). Over the entire study period, the area of the high chlorophyll waters expanded by 19% relative to the September 1997 conditions. The expansion of high chlorophyll waters contributed vastly to the general increase of Chl-*a* in the deep basin region of the SCS (Figure 4b). Considering that the 19% area expansion was accompanied by an 18% increase in the total amount of Chl-*a* in high chlorophyll waters (Figure 7b), it was not surprising that the 13-year trend revealed no significant change (but a small 4% decrease) in the concentration of area-averaged Chl-*a* (Figure 6c, solid black line). On the other hand, there was little change (5% decline) in the total Chl-*a* in the low chlorophyll waters (Figure 7a), which in combination with the 9% shrinkage of the low chlorophyll water area (Figure 6d, solid grey line) resulted in only a 2% increase in area-averaged Chl-*a* concentration in low chlorophyll waters (Figure 6c, solid grey line). As in the case of shelf and deep basin sub-regions, all trends showed variable rates of increase or decrease. For example, the expansion of the high chlorophyll waters was strongest in the first few years after the 1997–98 El Niño and gave away to a slow decline between 2007 and 2010 (Figure 6d, solid black line).

[25] Changes in spatial patterns were further examined using the approach of *Polovina et al.* [2008]. To investigate the spatial expansions of oligotrophic habitat in Pacific subtropical gyres, *Polovina et al.* [2008] compared the oligotrophic area during the winter season when the gyres were expanding most rapidly. Specifically, they compared the areas with surface chlorophyll less than or equal to 0.07 mg-Chl-*a* m^{-3} computed from the 1998 and 1999 winter mean to the areas based on the 2005 and 2006 winter mean. Following this approach, in Figure 5a we compared the extent of the low

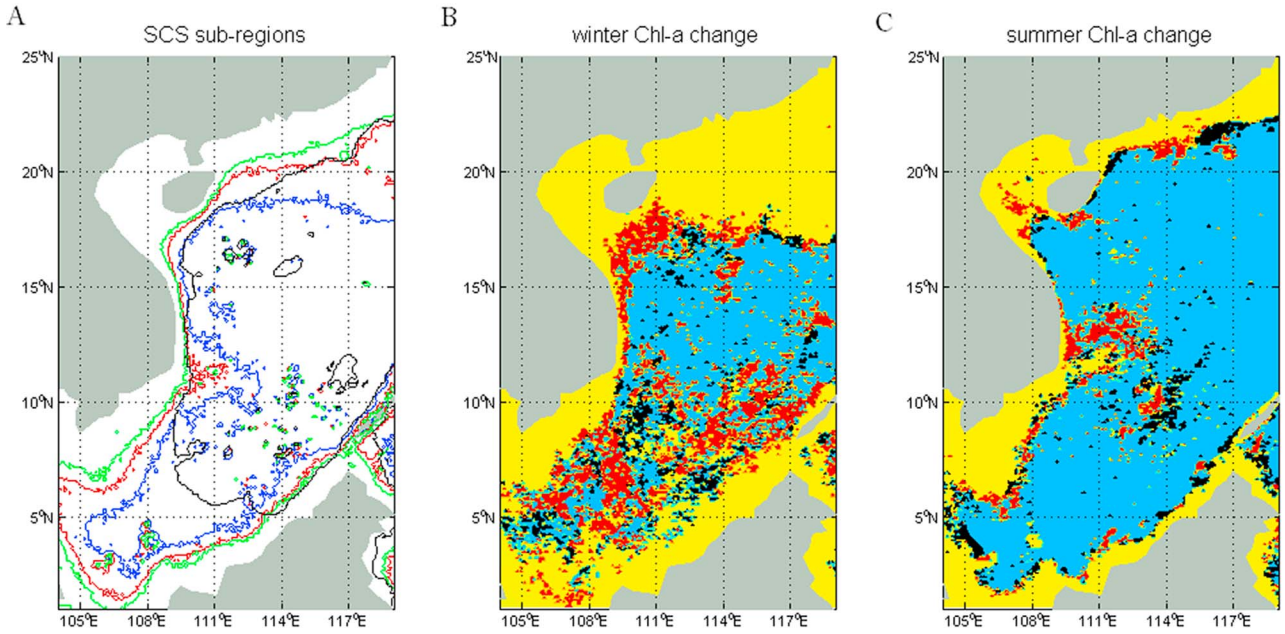

Figure 5. Distribution of low and high chlorophyll waters: (a) Location of Chl-*a* contours (0.15 mg m^{-3}-blue, 0.20 mg m^{-3}-red, 0.25 mg m^{-3}-green) vs the 500-m isobath (black), (b) January 1999/2000 vs 2009/2010 conditions, (c) August 1999/2000 vs 2008/2009 conditions. In Figures 5b and 5c red pixels mark those areas that became high chlorophyll waters at the end of the decade, while the black pixels mark those that became low chlorophyll waters. Light blue color corresponds to areas that maintained low Chl-*a* concentrations, while the yellow color corresponds to areas that maintained high Chl-*a* concentrations.

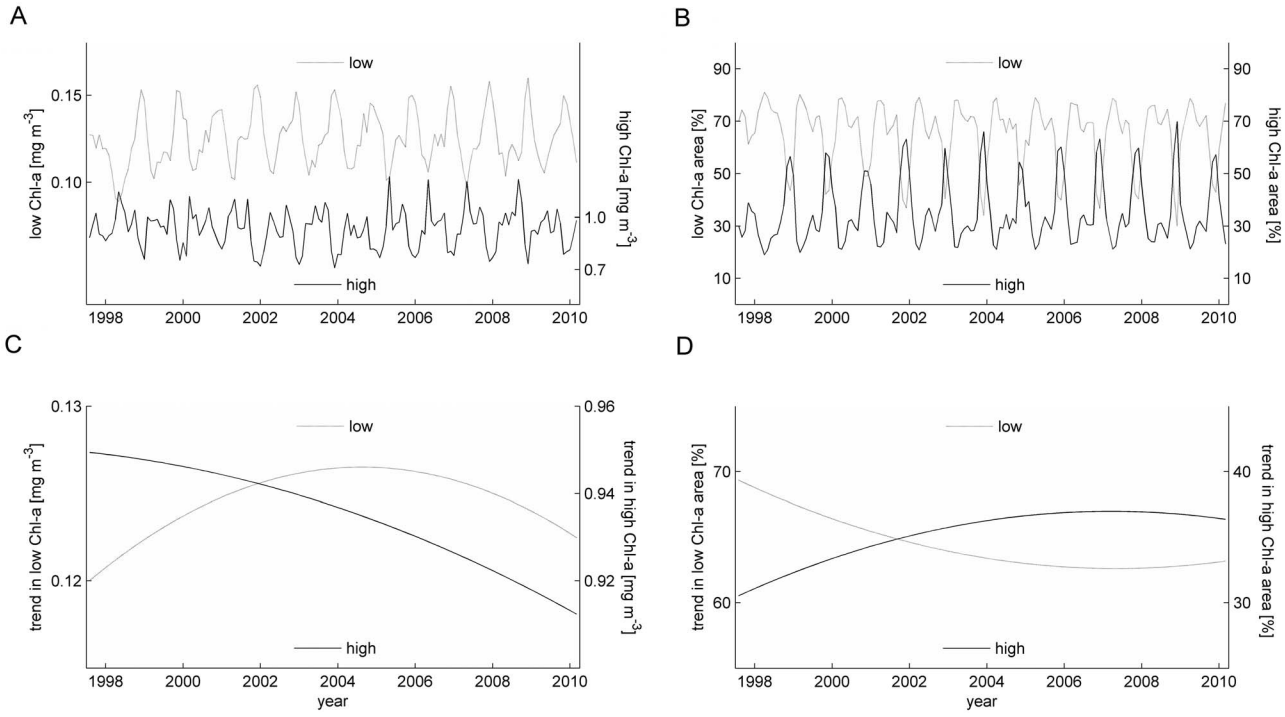

Figure 6. EEMD applied to the SeaWiFS Chl-*a* averaged over the low Chl-*a* region (grey solid line) and the high Chl-*a* region of the South China Sea (black solid line). (a and b) The original time series. (c and d) The residual trends after EEMD decomposition. Area averaged Chl-*a* concentration is in Figures 6a and 6c and the % of total area occupied by low and high Chl-a regions is shown in Figures 6b and 6d. Note: the percentage of low Chl-*a* and high Chl-*a* waters surface area adds to a 100%.

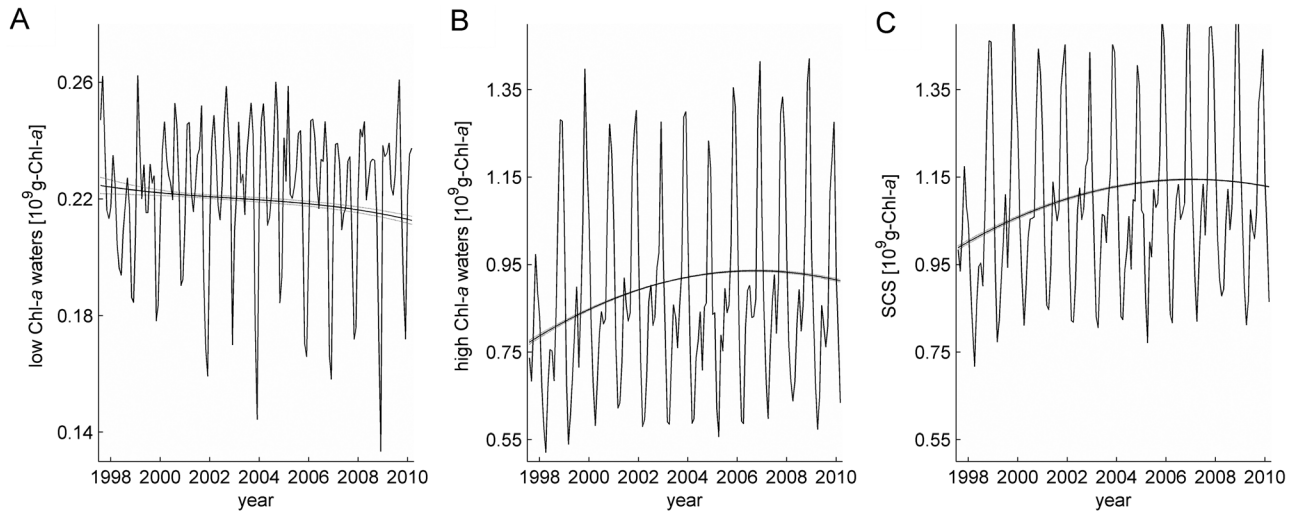

Figure 7. EEMD applied to the total amount of Chl-*a* [Gg of Chl-*a*] in the (a) low Chl-*a* region, (b) high Chl-*a* region, and (c) entire SCS. The original time series are shown together with the residual trends and the confidence limits (grey solid lines).

and high chlorophyll water in the SCS based on the climatological annual mean of 0.2 mg m^{-3} Chl-*a* contour. We determined the spatial extent of the low and high chlorophyll water from the 1999 and 2000 two winter mean and compared with its counterpart of 2009 and 2010 (Figure 5b). This procedure was repeated for 1999 and 2000 summer mean and 2008 and 2009 summer mean (Figure 5c). In Figure 8a we compared the extent of areas dominated by low and high surface wind speed in the SCS based on the climatological annual mean of 7 m s^{-1} contour. Consequently, we determined a 1999 and 2000 winter mean wind speed and compared it with the 2009 and 2010 winter mean (Figure 8b). Similarly, summer spatial patterns were determined from 1999 and 2000 summer mean and 2008 and 2009 summer

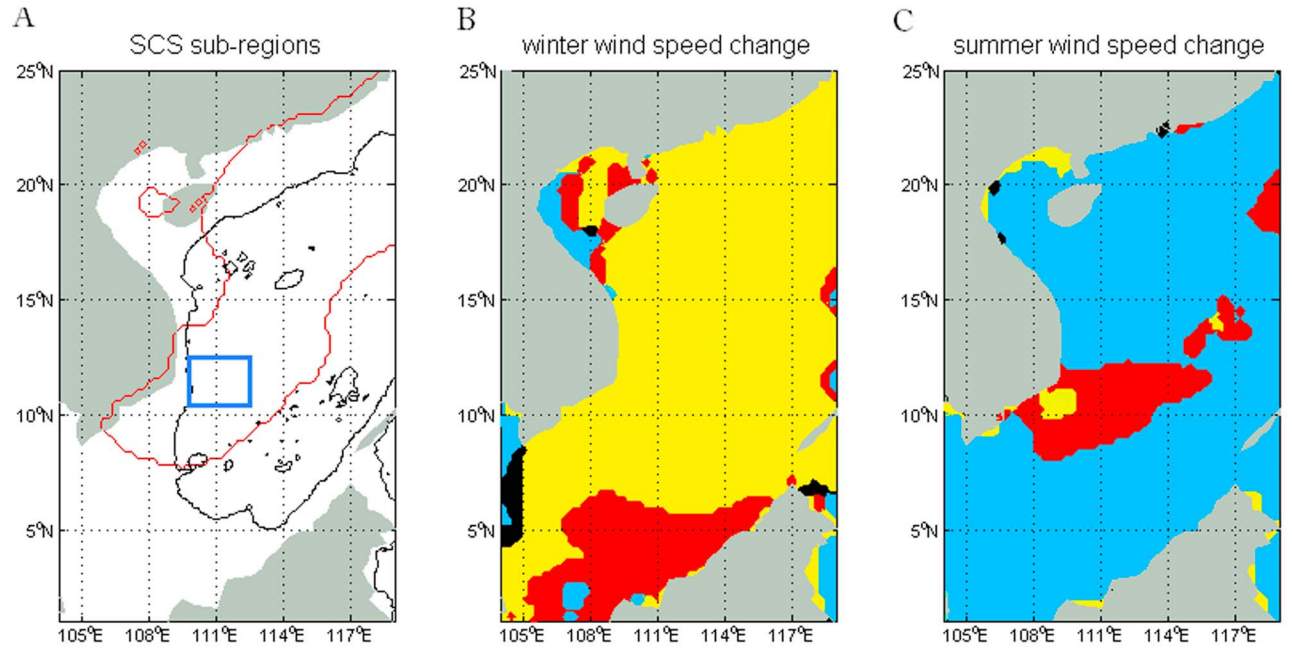

Figure 8. Distribution of low and high surface wind speed regions: (a) Location of 7 m s^{-1} surface wind speed contour (red) vs the 500-m isobath (black), the Vietnam upwelling region after *Zhao and Tang* [2007] is marked with a blue rectangle; (b) January 1999/2000 vs 2009/2010 conditions; (c) August 1999/2000 vs 2008/2009 conditions. In Figures 8b and 8c red pixels mark those areas that became high wind speed regions at the end of the decade, while the black pixels mark those that became low wind speed regions. Light blue color corresponds to areas that maintained low wind speed values, while the yellow color corresponds to areas that maintained high wind speeds.

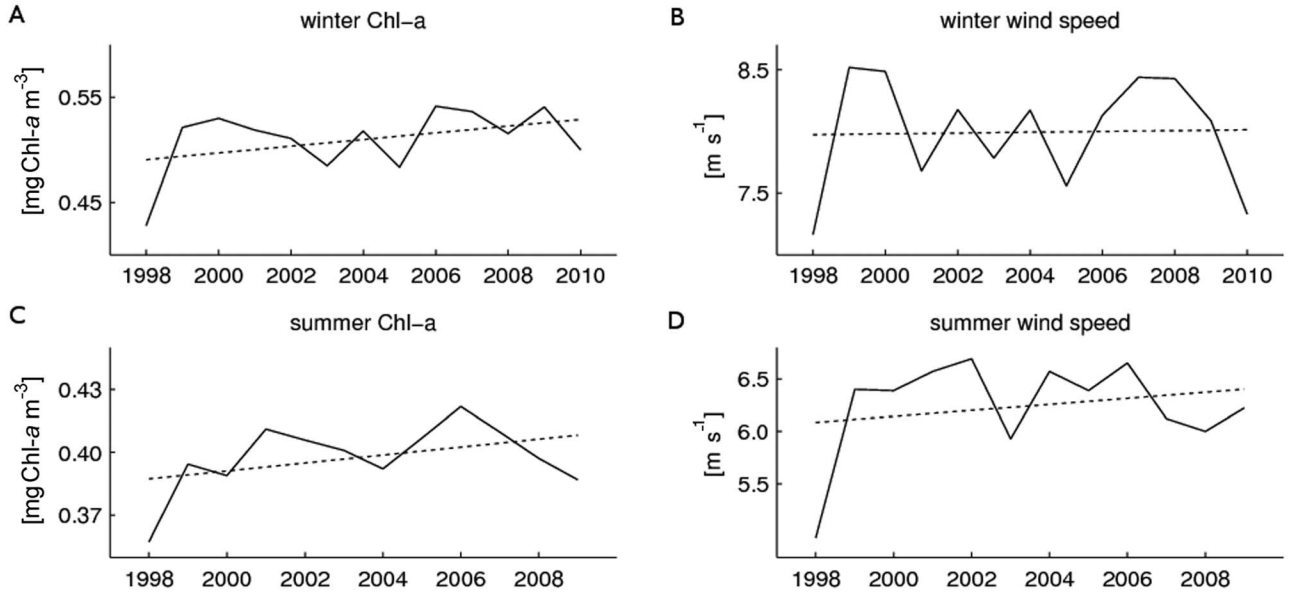

Figure 9. Linear regression analysis applied to the winter and summer Chl-*a* (Figures 9a and 9c) and surface wind speed (Figures 9b and 9d) time series. (a and b) The winter average time series between 1998 and 2010. (c and d) The changes in summer conditions between 1998 and 2009. Dotted lines represent the linear trends that were the best fit to the data.

mean conditions (Figure 8c). Winter and summer conditions were obtained from January and August month means, which were chosen because they represented the maximum winter and summer domain-averaged Chl-*a* concentrations identified in C2 in the EEMD analysis and were also in agreement with previous studies of seasonality of Chl-*a* in the SCS [e.g., *Liu et al.*, 2002].

[26] Figure 5b revealed that comparing to the 56% surface area of high chlorophyll waters in 1999 and 2000 mean, the surface area of high chlorophyll waters in 2009 and 2010 winter mean increased to 64%. The marked expansion of the red area in winter showed increased chlorophyll concentrations in the deep basin of the SCS, especially in the northwest fringe and across the central basin (Figure 5b). There was a similar pattern of expansion of the higher wind speed region (Figure 8b).

[27] Figure 5c showed that summer high Chl-a waters expanded from 28 to 30% of the SCS area over the decade. Despite the much smaller change in the extent of the high and low chlorophyll waters, expansion of the high chlorophyll area in the Vietnam upwelling zone was one spatial feature that stood out (Figure 5c). We marked the approximate location of the Vietnam upwelling region (11°–12.6°N, 110°–112°E) as defined by *Zhao and Tang* [2007] with a blue rectangle in Figure 8a. The increase in Chl-a concentration off the coast of Vietnam was coincident with an expansion of higher wind speeds in that region over the decade (Figure 8c). Although we expected the summer distribution of Chl-*a* to be primarily regulated by positive wind stress curl and upwelling, maps of wind stress curl were not spatially coherent and showed no significant trends. Mixing induced by stronger surface wind speeds was therefore the more likely cause of observed changes in Chl-a distribution, both in winter and summer. We concluded that the increase of the high chlorophyll area in winter appeared to contribute the most toward the large (20%) increase of Chl-*a* concentration in the deep basin region of the SCS.

3.3. Trends in Seasonal Distribution of Chl-*a* and Surface Wind Speed

[28] In order to verify the inter-annual link between the Chl-*a* and the surface wind speed, we performed linear regression analysis on the winter (mean of December, January and February) and summer (mean of June, July and August) time series averaged from the entire SCS basin (Figure 9). Although the strongest increase in the seasonal Chl-*a* maximum occurred between 1998 and 2000, the trend marked a continuous increase throughout the length of study period with the exception of summer 2009 and winter 2010 that drove the Chl-*a* values close to, or even below the decadal average in the case of summer Chl-*a*. The linear trends predicted an 8% increase in winter Chl-*a* and a 5% increase in summer Chl-*a* between 1998 and 2010. These rates match the increase in monthly and area-averaged Chl-*a* increase revealed by EEMD (9%). Detailed inspection of the yearly distribution of seasonal peaks suggested very different rates of increase (or decrease) at and in between the boundaries of the time series.

[29] Linear regression analysis of the seasonal wind speed showed no change in winter but a 5% increase in summer. A closer inspection of the wind speed seasonal time series revealed very low averaged wind speeds in winter 2009 and 2010 following a period of relatively stronger winds in 2007 and 2008. There were no such analogous declines in wind speed in the summer months of 2009 and 2010. We suspect that EEMD analysis performed on seasonally averaged wind speed time series; if long enough time series were available, it would have provided a more local and thus more accurate description of the inter-annual trend in surface wind speed. Nevertheless, Chl-*a* and surface wind speed were

significantly and positively correlated in both winter and summer, with respective correlation coefficients of 0.76 and 0.77 (Table 1). We did not find similar correlation between Chl-*a* and wind stress curl. However, as revealed in previous studies that investigated patterns of wind stress curl variability, summer upwelling areas of the SCS are susceptible to regional climate changes [e.g., *Xie et al.*, 2003; *Hong et al.*, 2009]. The upwelling region off the coast of Vietnam (Figure 8a) and changes in local wind stress curl were also often the focus in studying the role of ENSO and decadal variability in the SCS biogeochemistry [e.g., *Zhao and Tang*, 2007]. In order to discern between the effects of stronger vertical mixing and enhanced upwelling, we performed EEMD and linear regression on wind stress curl time series but found no consistent trend in the deep basin region of the SCS. We found a 20% increase in summer wind stress curl confined to the Vietnam upwelling region (not shown), consistent with the expansion of higher surface wind speeds onto that region (Figure 8c). Nonetheless, the small corresponding increase in the area-averaged Chl-*a* in that area made this result insignificant in the scale of the entire SCS basin.

4. Conclusions

[30] This study utilized a new data analysis tool that can effectively extract high to low frequency oscillations from oceanographic records and provide a residual trend that is more informative than a simple monotonic line obtained by means of linear regression. The results of EEMD applied to the SeaWiFS Chl-*a* and the satellite-derived wind speed in the SCS confirmed that the annual cycle, driven by the monsoon circulation, is the dominant factor in the temporal variability of Chl-*a* distribution. Moreover, the results indicated that the surface Chl-*a* concentration in the SCS increased between September 1997 and April 2010, exhibiting a variable rate of increase possibly related to the ENSO cycle. Changes primarily driven by the spatial expansion of high chlorophyll areas onto the deep basin were concurrent with the strengthening of wind speed. Such observations indicated a close link between changes in physical forcing and biogeochemical cycling, similar to the ones observed in other marginal seas [e.g., *Goes et al.*, 2005].

[31] In this study we concluded that while there was a visible trend in areal expansion of high Chl-*a* waters across the study period, the shape of this trend most likely resulted from two very strong El Niño events that occurred at the beginning and end of the time series. We suspect there is an overriding cycle of lower frequency associated with changes in the equatorial Pacific Hadley cell that control the decadal changes in the physical and biological coupling in the SCS. Although we linked the observed 13-year trends to the ENSO cycles, the Indian Ocean Dipole [*Saji and Yamagata*, 2003] or the recently described El Niño Modoki [*Ashok et al.*, 2007; *Chang et al.*, 2008] are among other sources of regional variability that have been shown to control the ocean-atmosphere coupling in the SCS. Recent modeling efforts utilized longer time series dating back to 1991 to investigate a possibility of a general regime shift in the SCS after the 1997–98 El Niño [*Chai et al.*, 2009; *Liu and Chai*, 2009; *Xiu et al.*, 2010]. However, without parallel in situ and remote sensing observations, it is difficult to draw conclusions with respect to biological cycling in particular.

[32] **Acknowledgments.** This research was supported by NASA and NSF grants to F. Chai, NSFC grants (90711006 and 2011CB403500) to H. Xue and F. Chai. We gratefully acknowledge the use of the SeaWiFS data obtained from the Goddard DAAC under the NASA auspices. The Blended Sea Winds data was obtained from NOAA NCDC. We further thank Peng Xiu and Andrew Thomas for their helpful comments, and two anonymous reviewers for greatly improving an earlier version of this manuscript. We thank Norden Huang greatly for making the HHT analysis code available.

References

Ashok, K., S. K. Behera, S. A. Rao, H. Y. Weng, and T. Yamagata (2007), El Nino Modoki and its possible teleconnection, *J. Geophys. Res.*, *112*, C11007, doi:10.1029/2006JC003798.

Balch, W. M., and C. F. Byrne (1994), Factors affecting the estimate of primary production from space, *J. Geophys. Res.*, *99*(C4), 7555–7570, doi:10.1029/93JC03091.

Chai, F., G. M. Liu, H. J. Xue, L. Shi, Y. Chao, C.-M. Tseng, W.-C. Chou, and K.-K. Liu (2009), Seasonal and interannual variability of carbon cycle in South China Sea: A three-dimensional physical-biogeochemical modeling study, *J. Oceanogr.*, *65*(5), 703–720, doi:10.1007/s10872-009-0061-5.

Chang, C.-W. J., H.-H. Hsu, C.-R. Wu, and W.-J. Sheu (2008), Interannual mode of sea level in the South China Sea and the roles of El Nino and El Nino Modoki, *Geophys. Res. Lett.*, *35*, L03601, doi:10.1029/2007GL032562.

Chao, S.-Y., P.-T. Shaw, and S. Y. Wu (1996), El Niño modulation of the South China Sea circulation, *Prog. Oceanogr.*, *38*(1), 51–93, doi:10.1016/S0079-6611(96)00010-9.

Chen, C.-C., F.-K. Shiah, S.-W. Chung, and K.-K. Liu (2006), Winter phytoplankton blooms in the shallow mixed layer of the South China Sea enhanced by upwelling, *J. Mar. Syst.*, *59*(1–2), 97–110, doi:10.1016/j.jmarsys.2005.09.002.

Chen, H., G. Fang, B. Yin, Y. Wang, and Z. Wei (2010), Forecasts of South China Sea surface temperature anomalies using the Niño indices and dipole mode index as predictors, *Chin. J. Oceanol. Limnol.*, *28*(1), 144–152, doi:10.1007/s00343-010-9197-9.

Chu, P. C., S. Lu, and Y. Chen (1997), Temporal and spatial variabilities of the South China Sea surface temperature anomaly, *J. Geophys. Res.*, *102*(C9), 20,937–20,955, doi:10.1029/97JC00982.

Goes, J. I., P. G. Thoppil, H. R. Gomes, and J. T. Fasullo (2005), Warming of the Eurasian landmass is making the Arabian Sea more productive, *Science*, *308*(5721), 545–547, doi:10.1126/science.1106610.

Gu, D., T. Li, Z.-P. Ji, and B. Zheng (2010), Connection of the South China Sea summer monsoon to maritime continent convection and ENSO, *J. Trop. Meteorol.*, *16*(1), 1–9, doi:10.3969/j.issn.1006-8775.2010.01.001.

Hong, H. S., C. Y. Zhang, S. L. Shang, B. Q. Huang, Y. H. Li, X. D. Li, and S. M. Zhang (2009), Interannual variability of summer coastal upwelling in the Taiwan Strait, *Cont. Shelf Res.*, *29*(2), 479–484, doi:10.1016/j.csr.2008.11.007.

Huang, N. E., and Z. Wu (2008), A review on Hilbert-Huang transform: Method and its applications to geophysical studies, *Rev. Geophys.*, *46*, RG2006, doi:10.1029/2007RG000228.

Huang, N. E., Z. Shen, S. R. Long, M. C. Wu, H. H. Shih, Q. Zheng, N.-C. Yen, C. C. Tung, and H. H. Liu (1998), The empirical mode decomposition and the Hilbert spectrum for nonlinear and nonstationary time series analysis, *Proc. R. Soc. A*, *454*, 903–995, doi:10.1098/rspa.1998.0193.

Huang, N. E., Z. Shen, and S. R. Long (1999), A new view of nonlinear water waves—The Hilbert spectrum, *Annu. Rev. Fluid Mech.*, *31*, 417–457, doi:10.1146/annurev.fluid.31.1.417.

Huang, N. E., M. L. Wu, S. R. Long, S. S. Shen, W. D. Qu, P. Gloersen, and K. L. Fan (2003), A confidence limit for the empirical mode decomposition and Hilbert spectral analysis, *Proc. R. Soc. A*, *459*, 2317–2345, doi:10.1098/rspa.2003.1123.

Jing, Z., Y. Qi, and Y. Du (2011), Upwelling in the continental shelf of northern South China Sea associated with 1997–1998 El Niño, *J. Geophys. Res.*, *116*, C02033, doi:10.1029/2010JC006598.

Klein, S. A., B. J. Soden, and N.-C. Lau (1999), Remote sea surface temperature variations during ENSO: Evidence for a tropical atmospheric bridge, *J. Clim.*, *12*, 917–932, doi:10.1175/1520-0442(1999)012<0917:RSSTVD>2.0.CO;2.

Kuo, N. J., C. R. Ho, Y. T. Lo, S. J. Huang, and C. C. Tsao (2008), Variability of chlorophyll-a concentration and sea surface wind in the South

China Sea associated with the El Niño-Southern Oscillation, paper presented at Oceans 2008 - MTS/IEEE Kobe Techno-Ocean, Inst. Electr. and Electr. Eng., Kobe, Japan.

Liu, A. K., Y. S. Chang, M.-K. Hsu, and N. K. Liang (1998), Evolution of nonlinear internal waves in the East and South China seas, *J. Geophys. Res.*, *103*(C4), 7995–8008, doi:10.1029/97JC01918.

Liu, G., and F. Chai (2009), Seasonal and interannual variability of primary and export production in the South China Sea: A three-dimensional physical-biogeochemical model study, *ICES J. Mar. Sci.*, *66*(2), 420–431, doi:10.1093/icesjms/fsn219.

Liu, K.-K., S.-Y. Chao, P.-T. Shaw, G.-C. Gong, C.-C. Chen, and T. Y. Tang (2002), Monsoon-forced chlorophyll distribution and primary production in the South China Sea: Observations and a numerical study, *Deep Sea Res., Part I*, *49*(8), 1387–1412, doi:10.1016/S0967-0637(02)00035-3.

MacMynowski, D. G., and E. Tziperman (2008), Factors affecting ENSO's period, *J. Atmos. Sci.*, *65*(5), 1570–1586, doi:10.1175/2007JAS2520.1.

Ning, X., F. Chai, H. Xue, Y. Cai, C. Liu, and J. Shi (2004), Physical-biological oceanographic coupling influencening phytoplankton and primary production in the South China Sea, *J. Geophys. Res.*, *109*, C10005, doi:10.1029/2004JC002365.

Ning, X., C. Lin, Q. Hao, C. Liu, F. Le, and J. Shi (2009), Long term changes in the ecosystem in the northern South China Sea during 1976–2004, *Biogeosciences*, *6*(10), 2227–2243, doi:10.5194/bg-6-2227-2009.

Polovina, J. J., E. A. Howell, and M. Abecassis (2008), Ocean's least productive waters are expanding, *Geophys. Res. Lett.*, *35*, L03618, doi:10.1029/2007GL031745.

Saji, N. H., and T. Yamagata (2003), Possible impacts of Indian Ocean dipole mode events on global climate, *Clim. Res.*, *25*(2), 151–169, doi:10.3354/cr025151.

Shaw, P.-T., and S.-Y. Chao (1994), Surface circulation in the South China Sea, *Deep Sea Res., Part I*, *41*(11–12), 1663–1683, doi:10.1016/0967-0637(94)90067-1.

Tang, D. L., H. Kawamura, T. V. Dien, and M. A. Lee (2004), Offshore phytoplankton biomass increase and its oceanographic causes in the South China Sea, *Mar. Ecol. Prog. Ser.*, *268*, 31–41, doi:10.3354/meps268031.

Tsui, P.-H., C.-C. Chang, and N. E. Huang (2010), Noise-modulated empirical mode decomposition, *Adv. Adaptive Data Anal.*, *2*(1), 25–37, doi:10.1142/S1793536910000410.

Wang, B., R. Wu, and T. Li (2003), Atmosphere-warm ocean interaction and its impact on Asian-Australian monsoon variability, *J. Clim.*, *16*, 1195–1211, doi:10.1175/1520-0442(2003)16<1195:AOIAII>2.0.CO;2.

Wang, B., F. Huang, Z. Wu, J. Yang, X. Fu, and K. Kikuchi (2009), Multi-scale climate variability of the South China Sea monsoon: A review, *Dyn. Atmos. Oceans*, *47*(1–3), 15–37, doi:10.1016/j.dynatmoce.2008.09.004.

Wong, G. T. F., T.-L. Ku, M. Mulholland, C.-M. Tseng, and D.-P. Wang (2007), The Southeast Asian Time-Series Study (SEATS) and the biogeochemistry of the South China Sea: An overview, *Deep Sea Res., Part II*, *54*(14–15), 1434–1447, doi:10.1016/j.dsr2.2007.05.012.

Wu, C. R., P. T. Shaw, and S. Y. Chao (1998), Seasonal and interannual variations in the velocity field of the South China Sea, *J. Oceanogr.*, *54*(4), 361–372, doi:10.1007/BF02742620.

Wu, Z., and N. E. Huang (2004), A study of the characteristics of white noise using the empirical mode decomposition method, *Proc. R. Soc. A*, *460*, 1597–1611, doi:10.1098/rspa.2003.1221.

Wu, Z., and N. E. Huang (2005), Ensemble empirical mode decomposition: A noise-assisted data analysis method, *Tech. Rep., 193*, Cent. for Ocean-Land-Atmos. Stud., Calverton, Md. (Available at ftp://grads.iges.org/pub/ctr/ctr_193.pdf.)

Wu, Z., and N. E. Huang (2009), Ensemble empirical mode decomposition: A noise assisted data analysis method, *Adv. Adaptive Data Anal.*, *1*(1), 1–41, doi:10.1142/S1793536909000047.

Wu, Z., N. E. Huang, S. R. Long, and C.-K. Peng (2007), On the trend, detrending, and the variability of nonlinear and non-stationary time series, *Proc. Natl. Acad. Sci. U. S. A.*, *104*(38), 14,889–14,894, doi:10.1073/pnas.0701020104.

Wyrtki, K. (1961), Physical oceanography of the south-east Asian waters, in *Scientific Results of Marine Investigations of the South China Sea and the Gulf of Thailand*, pp. 1–195, Scripps Inst. of Oceanogr., La Jolla, Calif.

Xie, S. P., Q. Xie, D. X. Wang, and W. T. Liu (2003), Summer upwelling in the South China Sea and its role in regional climate variations, *J. Geophys. Res.*, *108*(C8), 3261, doi:10.1029/2003JC001867.

Xie, S. P., K. Hu, J. Hafner, H. Tokinaga, Y. Du, G. Huang, and T. Sampe (2009), Indian Ocean capacitor effect on Indo-western Pacific climate during the summer following El Niño, *J. Clim.*, *22*(3), 730–747, doi:10.1175/2008JCLI2544.1.

Xiu, P., F. Chai, L. Shi, H. J. Xue, and Y. Chao (2010), A census of eddy activities in the South China Sea during 1993–2007, *J. Geophys. Res.*, *115*, C03012, doi:10.1029/2009JC005657.

Xue, H., F. Chai, N. R. Pettigrew, D. Xu, M. Shi, and J. Xu (2004), Kuroshio intrusion and the circulation in the South China Sea, *J. Geophys. Res.*, *109*, C02017, doi:10.1029/2002JC001724.

Xue, H., F. Nan, A. P. Palacz, L. Shi, F. Chai, and Y. Chao (2010), Decadal signals in the South China Sea–Is there a regime shift after the 97–98 El Niño?, *Eos Trans. AGU*, *91*(26), West. Pac. Geophys. Meet. Suppl., Abstract U32A–03.

Zhang, H.-M., R. W. Reynolds, and J. J. Bates (2006), Blended and gridded high resolution global sea surface wind speed and climatology from multiple satellites: 1987–present, paper presented at 2006 Annual Meeting, Am. Meteorol. Soc., Atlanta.

Zhao, H., and D. L. Tang (2007), Effect of 1998 El Niño on the distribution of phytoplankton in the South China Sea, *J. Geophys. Res.*, *112*, C02017, doi:10.1029/2006JC003536.

Zong, H. B., Y. G. Liu, P. Xiu, Q. Xu, and Z. R. Rong (2010), Interannual variability of latent and sensible heat fluxes in the South China Sea, *Chin. J. Oceanol. Limnol.*, *28*(1), 153–159, doi:10.1007/s00343-010-9241-9.

C. Armbrecht, F. Chai, A. P. Palacz, and H. Xue, School of Marine Sciences, University of Maine, Orono, ME 04469, USA. (artur.palacz@maine.edu)

C. Zhang, State Key Laboratory of Marine Environmental Science, Xiamen University, Fujian 361005, China.